NATIONAL ENERGY TECHNOLOGY LABORATORY

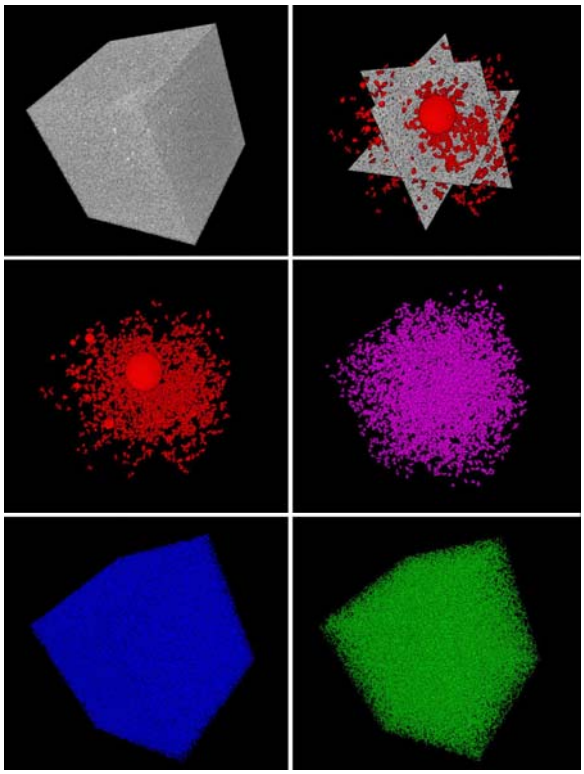

Computed Tomography and Statistical Analysis of Bubble Size Distributions in Atmospheric-Generated Foamed Cement

9 August 2013

U.S. DEPARTMENT OF ENERGY

Office of Fossil Energy

NETL-TRS-2-2013

Disclaimer

Cover Illustration: 3-D renderings of a $(10.4\ mm)^3$ digital subsection of 10% foam quality cement sample. (A) Opaque grayscale cement cube. (B) Orthoslices of solid cube with largest bubbles. (C) Largest bubbles in data set that sum to 10% of the total void space in the sample. (D) The next largest bubbles, summing again to 10% of the total void volume. (E) The mean bubbles, between the largest and the smallest in the sample set. (F) The smallest half of the bubbles.

Suggested Citation: Kutchko, B.; Crandall, D.; Gill, M.; McIntyre, D.; Spaulding, R.; Strazisar, B.; Rosenbaum, E.; Haljasmaa, I.; Benge, G.; Cunningham, E.; DeBruijn, G.; Gardner, C. *Computed Tomography and Statistical Analysis of Bubble Size Distributions in Atmospheric-Generated Foamed Cement*; NETL-TRS-2-2013; EPAct Technical Report Series; U.S. Department of Energy, National Energy Technology Laboratory: Morgantown, WV, 2013; p 28.

An electronic version of this report can be found at: http://netl.doe.gov/onsite_research

Computed Tomography and Statistical Analysis of Bubble Size Distributions in Atmospheric-Generated Foamed Cement

Barbara Kutchko[1], Dustin Crandall[2], Magdalena Gill[2], Dustin McIntyre[3], Richard Spaulding[1] (ORISE), Brian Strazisar[1], Eilis Rosenbaum[1], Igor Haljasmaa[4], Glen Benge[5], Erick Cunningham[6], Gunnar DeBruijn[7], Craig Gardner[8]

[1] U.S. Department of Energy, Office of Research and Development, National Energy Technology Laboratory, 626 Cochrans Mill Road, Pittsburgh, PA 15236

[2] U.S. Department of Energy, National Energy Technology Laboratory, URS, 3610 Collins Ferry Road, Morgantown, WV 26507

[3] U.S. Department of Energy, Office of Research and Development, National Energy Technology Laboratory, 3610 Collins Ferry Road, Morgantown, WV 26507

[4] U.S. Department of Energy, National Energy Technology Laboratory, URS, 626 Cochrans Mill Road, Pittsburgh, PA 15236

[5] Benge Consulting, 86 E Slatestone Circle, The Woodlands, TX 77382

[6] BP America, 501 Westlake Boulevard, Houston, TX 77079

[7] Schlumberger, 300 Schlumberger Drive, Sugar Land, TX 77478

[8] Chevron, 3901 Briarpark Drive, Houston, TX 77042

NETL-TRS-2-2013

9 August 2013

NETL Contacts:

Barbara Kutchko, Principal Investigator

Kelly Rose, Technical Coordinator

George Guthrie, Focus Area Lead

This page intentionally left blank

Table of Contents

List of Figures

Acronyms, Abbreviations, and Symbols

Term	Description
µA	Microampere, 10^{-6} amperes
µm	Micrometer, 10^{-6} meter
2-D	Two-dimensional
3-D	Three-dimensional
API	American Petroleum Institute
BSD	Bubble size distribution
CT	Computed tomography
FCG	Foamed cement generator
kV	Kilovolt, 1,000 volts
pF	Picofarad, 10^{-12} farad
RP	Recommended practice
SEM	Scanning electron microscopy

Acknowledgments

This work was completed as part of National Energy Technology Laboratory (NETL) research for the Department of Energy's Complementary Research Program under Section 999 of the Energy Policy Act of 2005. The authors wish to acknowledge Roy Long (NETL Strategic Center for Natural Gas and Oil) and Elena Melchert (DOE Office of Fossil Energy) for programmatic guidance, direction, and support.

The authors would like to thank Bryan Tennant, Karl Jarvis and Roger Lapeer for helping to make the CT scanner lab functional. A special thanks to Jim Fazio for superior laboratory assistance.

ABSTRACT

NETL researchers have produced the first high-resolution X-ray computed tomography (CT) three-dimensional (3-D) images of atmospheric-generated foamed cement across a range of foam qualities. CT imaging enabled the assessment and quantification of the foamed cement structure, quality, and bubble size distribution in order to provide a better understanding of foamed cement. Foamed cements are widely used for cementing wells requiring lightweight slurries, prevention of gas migration, or wells with high-stress environments. Ultimately, this research will provide industry the knowledge to ensure long-term well integrity and safe operation of wells in which foamed cements are used.

1. INTRODUCTION

Foamed cement is a gas-liquid dispersion that is created when a gas, typically nitrogen, is stabilized as microscopic bubbles within cement slurry (Harms and Febus, 1985; Nelson, 2006). Foamed cements are ultra-low-density cement systems that are used in formations that are unable to support the annular hydrostatic pressure of conventional cement slurries (Nelson, 2006; Harlan et al., 2001). The use of foamed cement for its lightweight density is well documented in literature (Benge and Poole, 2005; Harlan et al., 2001; White et al., 2000; Kopp et al., 2000; Frisch et al., 1999; Benge et al., 1996; Thayer et al., 1993; Harms and Febus, 1985). More recently, foamed cement use has expanded into regions with high-stress environments, for example, in deepwater operations and isolating fragile formations (Nelson, 2006; Rae and Lullo, 2004; White et al., 2000; Judge and Benge, 1998; Benge et al., 1996). Foamed cements are used extensively when lost circulation zones, depleted zones, or low formation fracture gradients are encountered and a low-density cement system is required (Frisch et al., 1999; Thayer et al., 1993). It is often the cement system of choice for shallow flow conditions in the Gulf of Mexico (as outlined in API RP 65) and is used to prevent compaction damage in deepwater operations (Taiwo and Ogbonna, 2011; Harlan et al., 2001; White et al., 2000; Kopp et al., 2000; Moore et al., 2000; Frisch et al., 1999; API, 2010). Current technology allows for the ability to change the foamed cement density at the rig site without affecting slurry properties and does not have the pressure limitations found with ultra-lightweight extenders (Benge and Poole, 2005). In addition to its light-weight application, foamed cement has a unique resistance to temperature and pressure-induced stresses. In comparison to conventional cement, foamed cement is ductile and will deform when the casing is pressurized (Kopp et al., 2000). As such, foamed cements are often used to prevent stress cracking in the cement sheath due to temperature and pressure cycles (Benge et al., 1996). Foamed cement is claimed to exhibit superior fluid displacement, minimal shrinkage (and hence, gas-migration control), and long-term sealing through resistance to cement-sheath stress cracking (White et al., 2000).

Bubble size distribution can be an indicator of foamed cement stability (de Rozieres and Ferriere, 1991; Nelson 2006). A stable foamed cement is one in which the density or distribution of bubbles stays consistent throughout the cement. A stable foamed cement has a uniform distribution of distinct bubbles to ensure that gas will not break out of the slurry (Griffith et al., 2004). If the foamed cement is unstable, gas can coalesce and bubbles will increase in size, causing gas pockets to form and rise in the cement column. Unstable foams can result in uncemented sections caused by channeling in the well and density inhomogeneity (de Rozieres and Ferriere, 1991). It is important to note that the gas volume of the foam cement is referred to as the foam quality. The higher the foam quality, the higher the entrained gas content (e.g. 20% foam quality contains 20% nitrogen or air by volume).

There is a significant knowledge gap regarding the stability and properties of foamed cement as it is placed in the well, and as well as post-placement (Kutchko et al., 2012). Designing foamed cement systems requires an understanding of the influence of parameters such as temperature, pressure and shear. Few published laboratory studies exist that examine foamed cement under wellbore conditions (de Rozieres and Ferriere, 1991). De Rozieres and Ferriere (1991) designed a foam generating unit to study foamed systems at a pressure range from 0.1 to 7 MPa (14.5 to 1015 psi). The samples were depressurized before analysis. The authors used scanning electron

microscopy (SEM) and mercury porosimetry to measure the BSD of foamed cements. In addition, the authors measured permeability, compressive strength, setting time, and fluid loss. The de Rozieres and Ferriere (1991) study concluded that foams generated at 7 MPa (1,015 psi) have smaller bubbles and a narrower BSD than foams generated at lower pressures. Foamed cements with a broader BSD were observed having higher compressive strengths than those with the same density, but smaller bubbles and permeability was found to increase with foam quality (de Rozieres and Ferriere, 1991).

Depressurizing a pressure-generated foamed cement can result in changes to the physical and geotechnical properties and cause irreversible damage of the bubble structure and distribution. This limits the validity of using atmospheric testing techniques. This research study builds on the work presented by de Rozieres and Ferriere (1991) in that an industrial CT scanner is utilized to obtain BSD and 3-D image datasets of atmospheric- and pressure-generated cement foams across a range of foam qualities. This report is a Part 1 of 3, in which the results of the atmospheric-generated foamed cements are discussed. Part 2 will assess and quantify the foam structure and quality of foamed cements collected utilizing the same full scale industrial equipment and methodology used to generate cement in a well. Part 3 will detail laboratory-generated foamed cements using the Schlumberger foamed cement generator (FCG). The FCG is the same unit used in the de Rozieres and Ferriere (1991) study. As a result, the 3-D images and data sets generated from the in situ CT scans will be directly compared to the 2-D SEM images from de Rozieres and Ferriere (1991). Both the field-generated and the laboratory-generated cements will be scanned at the same pressure in which they were generated using the industrial CT scanner. Thus, Part 1 serves to offer baseline evaluations of foamed cement at atmospheric conditions, whereas Parts 2 and 3 build on Part 1 by evaluating in situ properties of foamed cement. This correlation will provide a better understanding of the effects that foam cement production, transport downhole, and delivery to the wellbore annulus have on the overall sealing process. The results of this research will ultimately provide researchers, regulators, and industry the knowledge to ensure the safe operation and integrity of wells in which foamed cement systems are used.

2. METHODS

2.1 CEMENT SLURRY PREPARATION

Cement samples were prepared using a base slurry of Class H Portland cement (Lafarge, Joppa, IL) with a slurry density of 16.5 lbm/gal (1.97 g/cm^3). Class H was selected as it is the most common cement type used in the Gulf of Mexico. Foamed cement samples were prepared according to API RP 10 4-B using an Ametek (Chandler Engineering) constant speed mixer (model 30-60). Once the base slurry was mixed it was poured into a stainless steel, screw-top blender with a stacked blade assembly. Atmospheric foamed cements contained predefined amounts of air, as a percentage of the total cement volume. Four foam qualities: 10%, 20%, 30%, and 40% entrained air fractions were mixed using an industry standard foaming agent. Once mixed, the slurries were poured into 945 ml containers and were allowed to cure for 3 days under atmospheric conditions. One inch diameter cement cores were subsectioned using a Powermatic variable speed wet drill using a 1-in diamond-tipped core drill bit. The cored samples were next cut to a length of 2 in and the ends of the samples were cleaned using a Struers Secotom-10 wet saw. For consistency, the samples were labeled, weighed, and put in a desiccator to dry. Subsequent measurements of weight were taken until the weight remained consistent thus ensuring the samples were sufficiently dry for gas permeability measurement (Mindess and Young, 1981). All samples were dried at atmospheric pressure and temperature to avoid damaging them by thermally stressing or over desiccating, and thus ensuring quality results (Nelson, 2006).

2.2 CEMENT CORE PREPARATION

One-inch diameter cores of the 10%, 20%, 30%, and 40% foam qualities were drilled for scanning. These cores were subsequently subcored, at a 0.6 cm diameter, for use in higher resolution scans. In total eight scans were performed, four lower resolution scans of larger cores, and four higher resolution scans of subcores. Radial and axial photographs of these cores are shown in Figures 1, 2, 3, and 4. Each photograph includes a millimeter ruler for scale. In Figure 1, the 10% foam quality sample, the entrained air is not visibly apparent to the naked eye. Larger, "vug-like" air voids are noticeable in one of the samples. This is a common artifact in the mixing and pouring process. The 20% foam quality sample shown in Figure 2 has more apparent homogenous bubble structure, though still difficult to discern to the naked eye. In Figure 3, the 30% foam cement sample, the void space is much easier to see, while the 40% gas sample shown in Figure 4 can immediately be identified as a foamed cement sample due to the large number of voids.

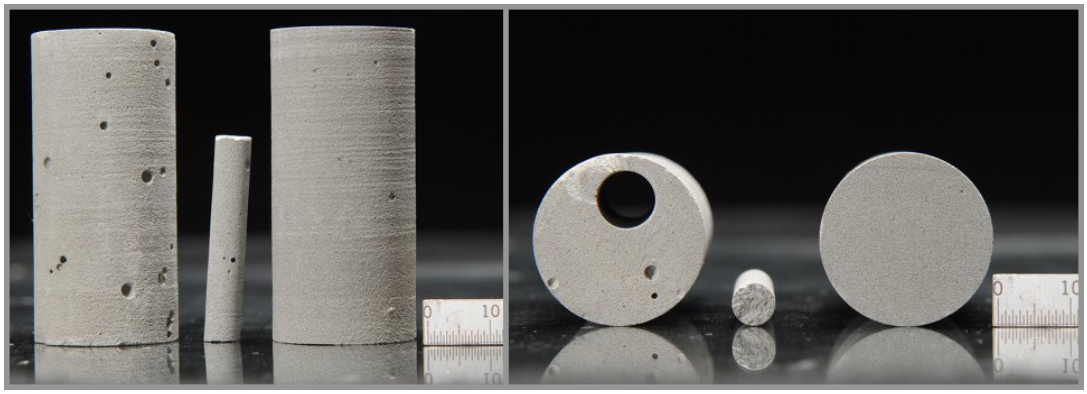

Figure 1: Photographs of the 10% foam quality subcores, 25.4 and 6 mm diameter.

Figure 2: Photographs of the 20% foam quality subcores, 25.4 and 6 mm diameter.

Figure 3: Photographs of the 30% foam quality subcores, 25.4 and 6 mm diameter.

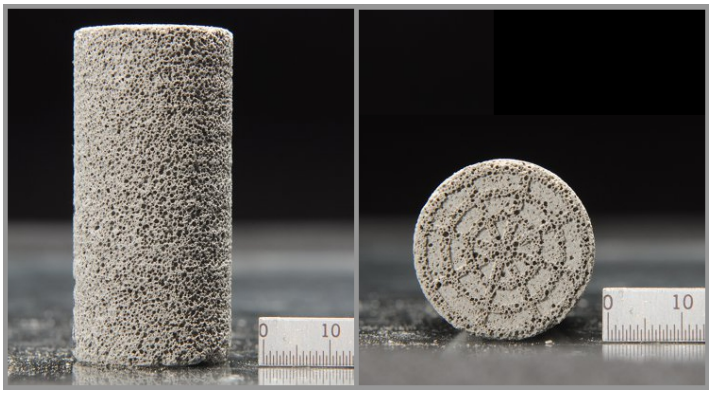

Figure 4: Photographs of the 40% foam quality subcore, 25.4 mm diameter. Artifact on bottom of core is due to the shape of the fluid distribution end cap to the core holders used to test the permeability.

2.3 CT SCANNING

All the cores were scanned in the North Star Imaging M-5000 industrial CT scanner. The scans were performed at two different magnification levels, all with an X-ray source voltage of 180 kV, and a tube current of 133.3 µA, for a total X-ray power of approximately 24 W. This low power level allowed the system to utilize a very small spot size, approximately 3µm, which can help to provide highly detailed and crisp images. For each 3-D scan 1,440 projections were obtained as the sample rotated on the sample stage, with 5 radiographs averaged for each projection. The reconstructed images of the 1-in-diameter cores have a voxel resolution of 13.5 µm. Smaller sub-cores with a 0.6-cm-diameter were scanned at a higher magnification and resulted in reconstructions with a voxel resolution of 3.7 µm. Figure 5 is a photograph of the NSI M-5000 industrial CT scanner at the National Energy Technology Laboratory (NETL) in Morgantown, West Virgina.

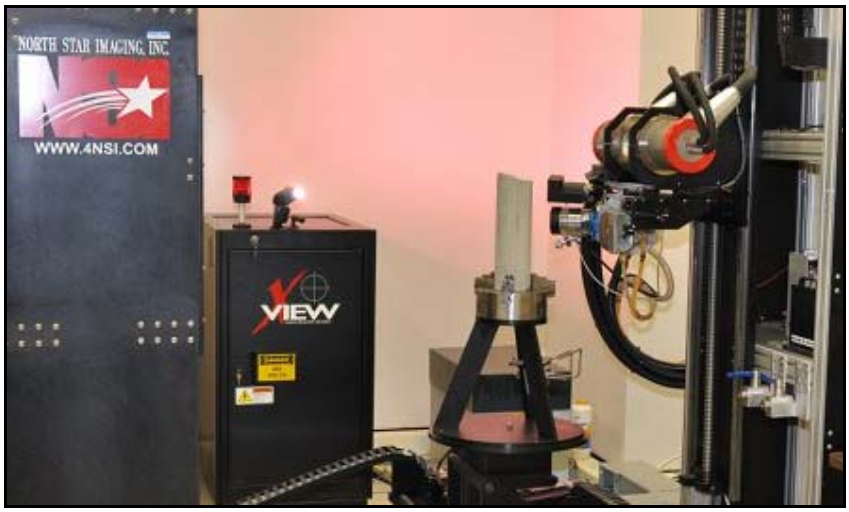

Figure 5: Photograph of the North Star Imaging M-5000 industrial CT scanner at the NETL in Morgantown, WV. X-ray source is shown on the right, a sandstone sample is vertically resting on the sample stage in the center, and the X-ray detector is on the left side of the photograph.

CT radiographs were reconstructed into a volume using North Star Imaging's industrial CT software, efX-CT. By initially processing 'calibration images' of high-density bearings rotating around the sample stage axis, efX-CT develops a set of algorithms that combine the two-dimensional (2-D) radiographs obtained from the CT scanning process into a three-dimensional (3-D) digital volume. This initial reconstruction can then be shifted to account for any small variations in the starting and ending positions of the physical rotation of the samples. A similar fine-tuning process is possible once the gross reconstruction settings are established. When the reconstruction properties of the image are set to provide the highest fidelity rendition of the scanned sample, as determined by the user, efX-CT constructs a 3-D volume of the object. The data is exported as a series of 16-bit grayscale cross-sectional tiff images of the core. Image post processing is performed using the open-source software ImageJ (Rasband, 2012). In order to extract features of interest for quantitative volumetric analysis, images are segmented based on the variation of grayscale values for different materials.

Porosity in cement falls into a range of types and sizes (Hover, 2011). Figure 6 illustrates the approximate size ranges that pores fall into. Much of the inherent porosity is microscopic in size, falling into the micropore, mesopore, macropore, and capillary pore categories. These pores, with the possible exception of the very largest of capillary pores, are below the detection range of the highest resolution scans obtained during this project, and cannot be resolved in the CT images. High-resolution CT scans in this study can resolve pores as small as 3.5 μm. Because of the use of repeatable cement formulas all properties of the unfoamed cement matrix, including its microporosity network, are assumed to be largely constant across the analyzed samples. Based on the pore size distribution, it can be assumed that air voids (≥ 10 μm) are the principal pore structures being detected and analyzed in this study.

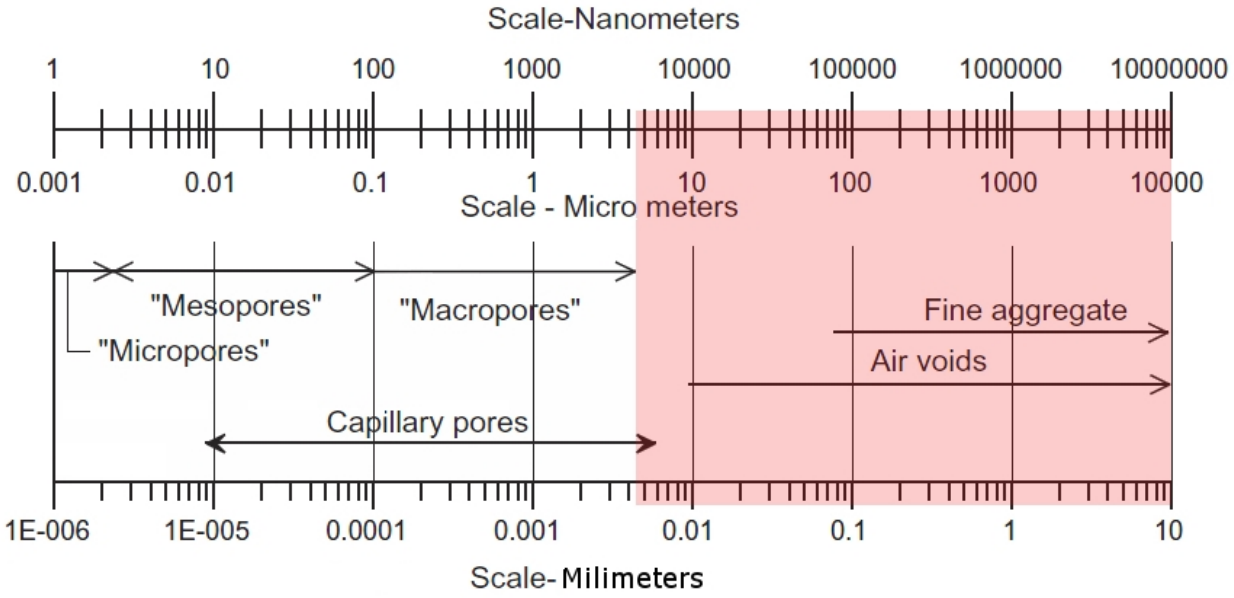

Figure 6: Approximate ranges of pores and other microscopic features in hardened cement. Range of CT scan resolutions obtained in this study is highlighted in red. Figure adapted from Hover (2011).

2.4 DIGITAL IMAGING AND STATISTICAL ANALYSIS

In X-ray CT scans, grayscale values of the final image are based on the amount of attenuation produced as the X-ray travels through matter. The degree of attenuation that occurs in a given material is defined as the absorption coefficient, which is largely controlled by the density and the effective atomic number of the material. In practice absolute grayscale values can be further influenced by a range of environmental variables and often vary from scan to scan. Experimental factors such as room temperature and how long the CT scanner has been running can influence the results. Additional factors are the energy of the penetrating X-rays, because absorption coefficients vary strongly with peak X-ray energy. Post-scan image processing and segmentation, where choice and application of appropriate thresholds is of paramount importance, requires scientific rigor to achieve consistent, repeatable, and statistically significant results.

Of the variety of automated thresholding algorithms that exist, many are based on histogram compilations of an entire image, which are then separated into two classes of pixels to create a binary image. For many natural samples, including cement, image pixels can belong to more than two classes, representing more than two different materials (Arora et al., 2008; Osuna-Enciso et al., 2013). For the foamed cement scans these classes are, in order from highest to lowest grayscale values, dense particles in the cement matrix, the cement matrix itself, pore fluids, and air. The relative amounts of each of these materials can skew a binary threshold histogram and cause an automated thresholding processes to be affected. The variation in material that has been observed in the cement CT scans can be seen in Figures 7 and 8, where 2-D slices of two different resolution scans of each foam quality cement sample are shown. In these grayscale CT images the darker regions indicate low-density material, i.e. void space in the cement. As can be seen, the overall darkness of the images varies, which is an indication that the mean grayscale value of the samples changes from scan to scan. High-density matrix material can be observed in the slices as well; these are the brighter voxels within the images.

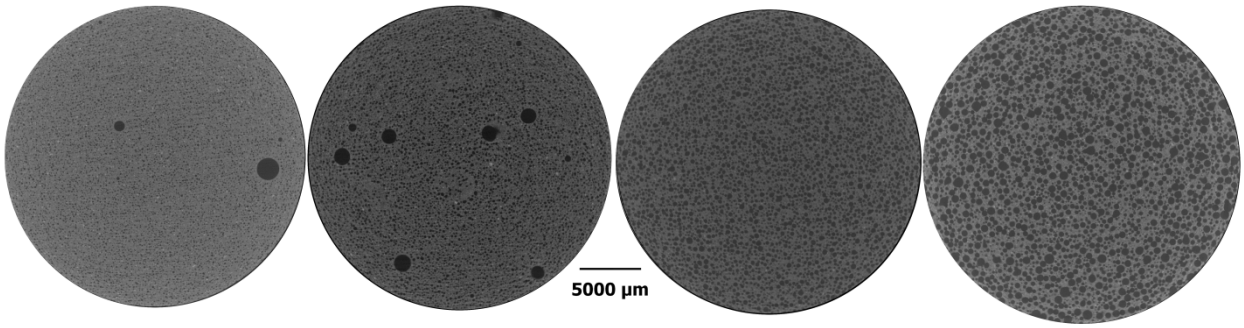

Figure 7: 2-D slices of reconstructed 13.5 µm resolution CT scans taken of the 1 in diameter samples of foamed cement with a foam quality of 10%, 20%, 30%, and 40%, from left to right.

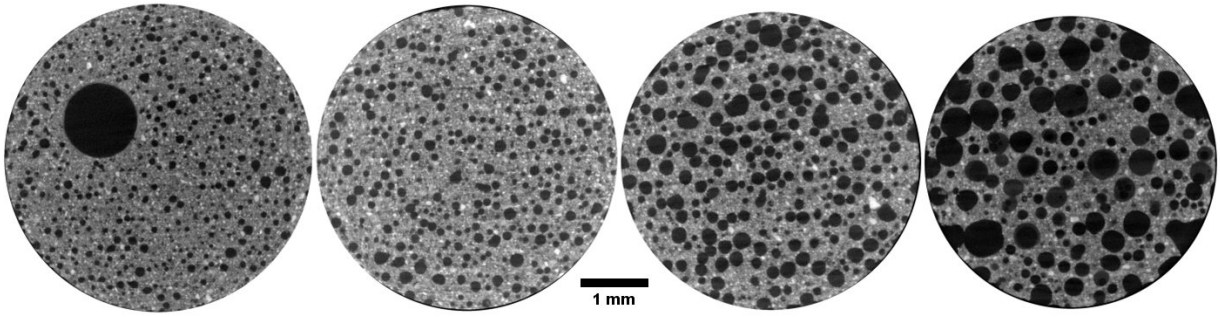

Figure 8: 2-D slices of reconstructed 3.7 µm resolution CT scans taken of the 0.6 cm diameter sub-samples of foamed cement with a foam quality of 10%, 20%, 30%, and 40%, from left to right.

Additionally, occasional artifacts of the CT process can further skew the overall histogram. Artifacts can arise from high-attenuation materials, reconstruction algorithm errors, and image acquisition oversights (Barrett and Keat, 2004). Often times a careful examination of an image sequence by a human being is the most efficient way to detect image artifacts.

The following segmentation procedure was developed by this research team to circumvent non-repeatability and false-positive issues. For this study the grayscale values were separated into two groups representing the cement matrix and the void space. A single threshold value was determined by sampling a number of representative images from the scan, selecting numerical values representing the two features being segmented, and calculating the mean grayscale value for each one. In fully dry cement samples these two features are cement matrix and air, while in wet samples they are cement and the pore fluid. Fewer individual measurements may be used in more homogenous materials and in less noisy scans, while a larger number of measurements are recommended in materials with more heterogeneity or higher amounts of scan noise. Typically, several hundred values will yield statistically significant results. The two average grayscale values were compared using a t-test to ensure their difference is statistically significant (Figure 9). The midpoint value between the two mean grayscales was taken to be the separation threshold. Bubble volumes are calculated from the extracted image by using the ObjectCounter3D ImageJ plugin (Bolte and Cordelières, 2006) to obtain the total number of voxels in each void. The scan resolution was used to convert the digital voxels to volumes.

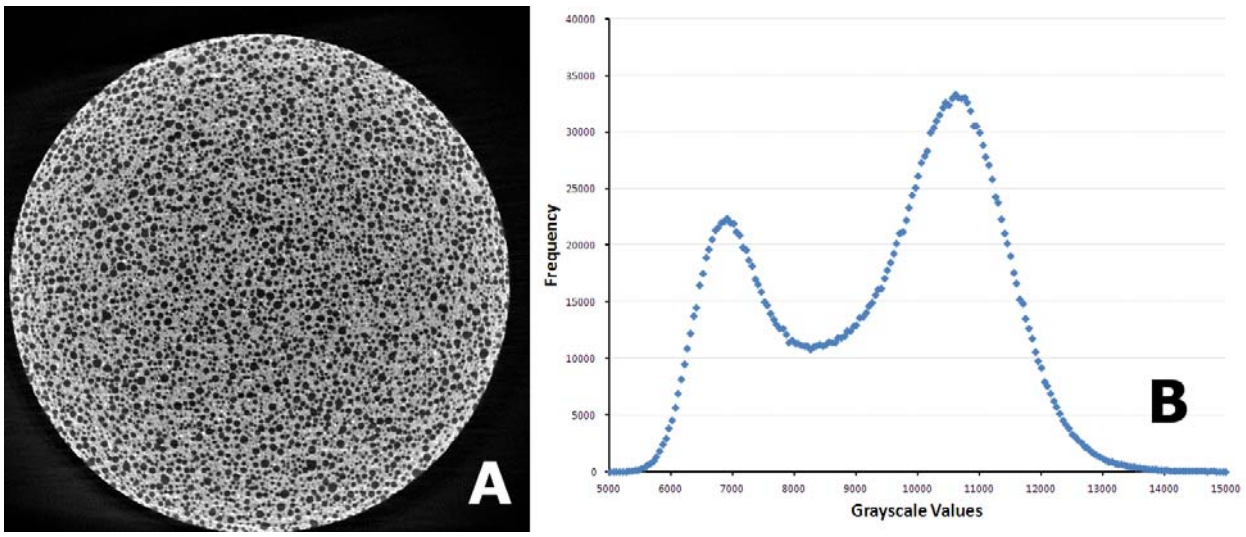

Figure 9: (A) Single slice of a 20% foam quality cement. (B) Bimodal distribution of grayscale values in this sample image.

A small subsection of the scan was chosen for detailed numerical analysis on bubble distribution. The limiting factor on sample size was the large amount of processing power necessary for the volume analysis. Volumes of approximately 0.8–0.9 cm^3 were analyzed for the low-resolution scans, and approximately 0.013 cm^3 for the high-resolution scans. For the 10% entrained air volume scans edge-adjacent bubbles were eliminated from the analysis, in order to eliminate partial bubble volumes. For foam qualities of 20–40% the increasingly interconnected nature of bubbles prevented such selection of data, and edge-adjacent bubbles had to be retained for analysis.

There is a possibility that the smallest isolated "bubble" volumes may be due to noise in the scan. To attempt to quantify what effect the smallest bubbles have on the overall bubble distribution a comparison was conducted on a sub-section of the 10% foam quality cement scan of bubbles with and without the smallest bubbles. Figures 10 and 11 illustrate bubble distributions for the 10% foam quality cement including and excluding all volumes under 10 voxels in size. Figure 10 shows the change in the distribution of bubble volumes if bubbles less than 10 voxels are excluded from the analysis of a scan with a voxel resolution of 13.5 µm. In total 19,877 data points were not accounted for in the plot shown in Figure 10(A). This is 16% of the total number of bubbles identified; 19,877 out of 124,188 total. However, as can be seen in Figure 10, the overall distribution of bubbles is not affected. In addition, because these potential bubbles are so small, the total amount of void space of these combined "less than 10 voxel bubbles" is a mere 0.2% of the total void space in the sample; $1.40(10^8)$ μm^3 out of $7.02(10^{10})$ μm^3. Because of the low total percentage of void space potentially neglected, the lack of change in the overall trend in the bubble distribution, and the removal of unquantifiable small noise from the analysis, the removal of 'voids' less than 10 voxels in volume was conducted for all other analysis presented in this report. Figure 11 shows similar results as Figure 10, but with a higher resolution data set of the same sample. Bubble volumes in both Figures 10 and 11 were divided into bin sizes of 50,000 μm^3 for consistency during comparisons. In order to further characterize the smallest 'void space' which should be omitted from the analysis, an unfoamed cement sample will be CT scanned under the same conditions as the foamed cements. The minimal amount of entrapped air

in an unfoamed sample would enable a minimum cutoff volume to be established for the quantification of noise in these scans.

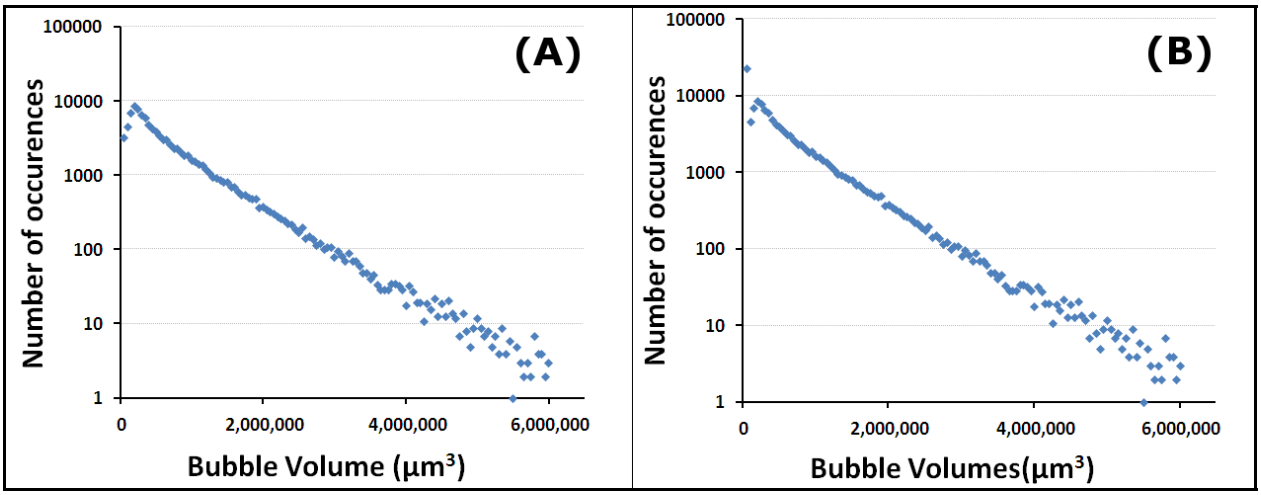

Figure 10: Bubble distributions in 13.5 µm resolution scan of a 10% foam quality cement. Data sorted into 50,000 µm^3 bins and the largest 70 volumes are not shown for graphical clarity. (A) Bubbles less than 10 voxels were excluded. (B) All data included.

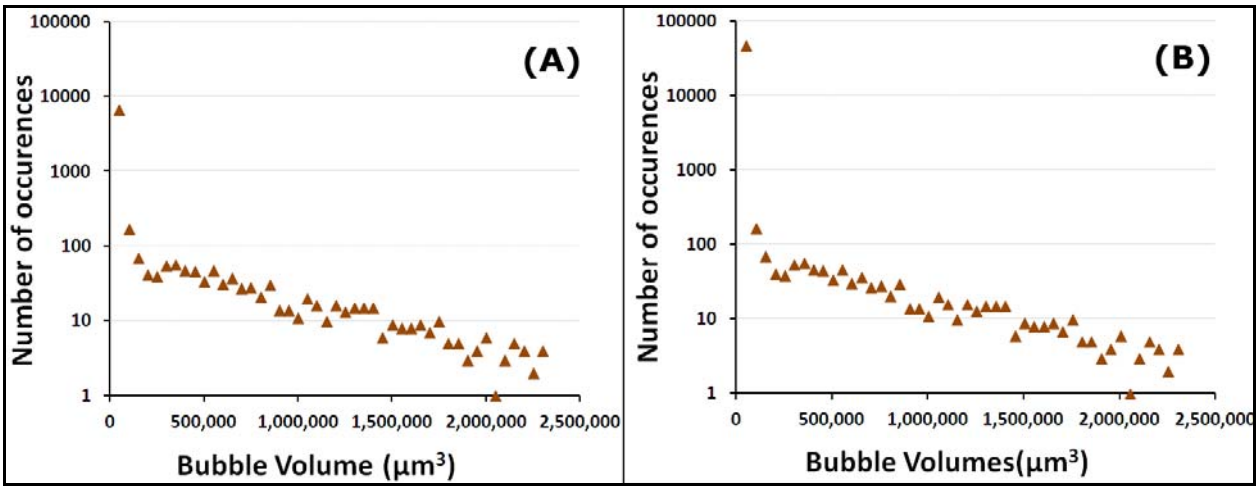

Figure 11: Bubble distributions in 3.7 µm resolution scan of 10% foam quality cement. Data sorted into 50,000 µm^3 bins and the largest 88 volumes are not shown for graphical clarity. (A) Bubbles less than 10 voxels were excluded. (B) All data included.

Another aspect of the analysis that deserves further examination after this pilot study is the effect of binning size on distributions of bubbles. As is shown in Figure 12, by using a smaller bin to collate the raw bubble volume data a larger number of data points are obtained. However, as has been discussed in the literature (Milojević, 2010), discrete data that appears to follow a power-law relationship is typically noisy at large values. This is seen in Figure 12(B) where the majority of bubble volumes greater than 100,000 µm^3 appear less than 5 times when placed in the smaller (500 µm^3) bins and the "clean" distribution of the data shown in Figure 12(A) is not apparent. While there is an increase in the number of data points with a smaller binning volume,

it is still unclear what binning of the data will be most effective to understand the underlying physical attributes of greatest importance to the foamed cement properties.

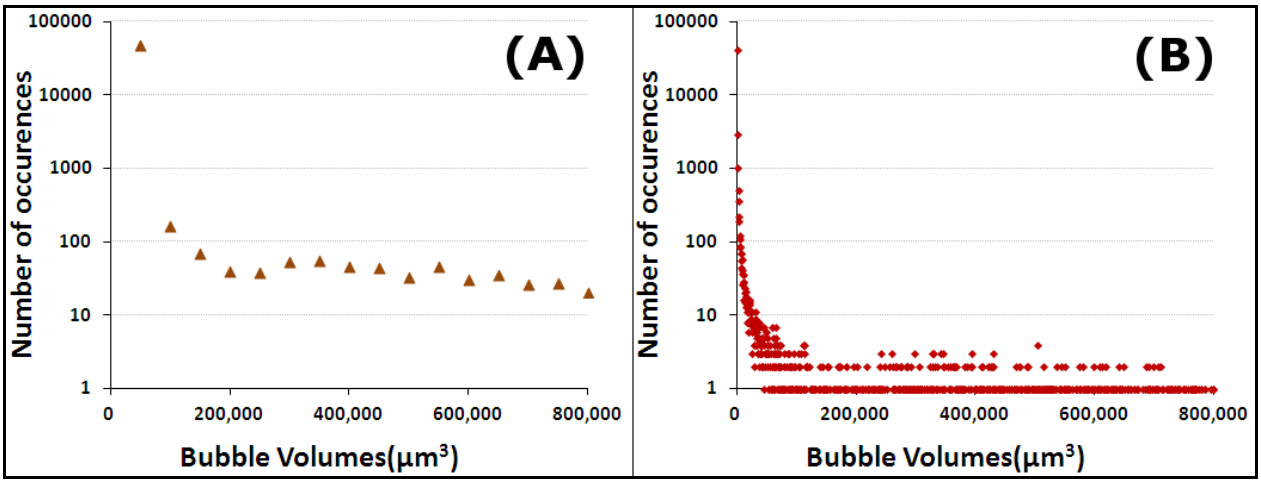

Figure 12: Bubble distribution in 3.7 µm resolution scan of 10% foam quality cement. Bubbles greater than 800,000 µm^3 are not plotted. (A) Data sorted in 50,000 µm^3 bins. (B) Data sorted in 500 µm^3 bins.

3. RESULTS

To test the accuracy of CT derived image data, the experimentally determined porosity of the cement samples was compared to porosity data derived from CT images (Figure 13). The correlation between the experimental gas fraction and the measured CT air volume was remarkably good. For 10 and 20% entrained air cements, the calculated porosity values were within 1% of experimental gas volume percentages. For the higher 30 and 40% foam quality cements, the measured porosities overestimated the air percentage, with the highest mismatch recorded for the low-resolution scan of 40% foam quality cement, where the CT scan calculated porosity was 46.22%. Predictably, the higher resolution scans provided a more accurate estimate of entrained air.

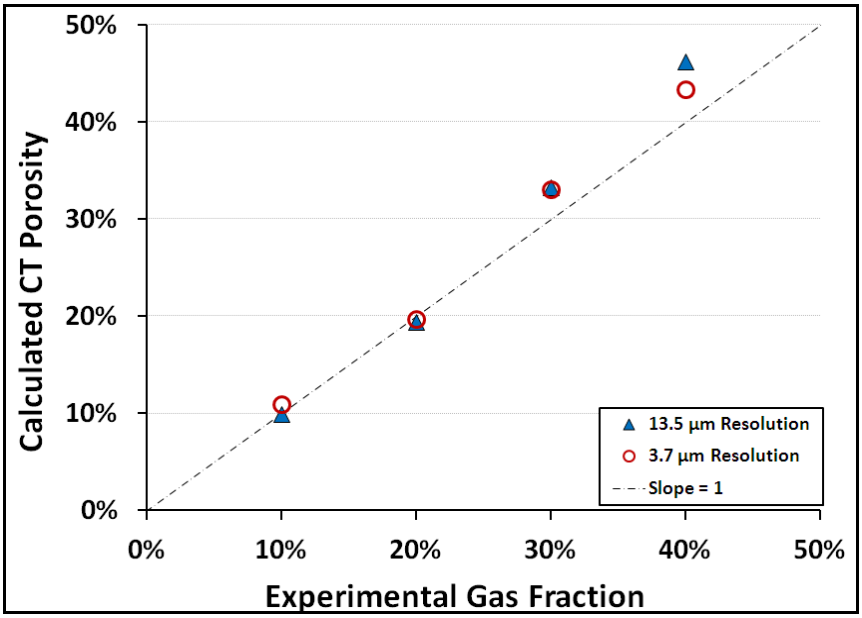

Figure 13: Comparison of CT-derived porosity to entrained air fraction, with the dashed line denoting a linear relationship with slope = 1. Results from low- and high-resolution scans are included.

Because of the apparent power law behavior between the void space distribution and volume shown in Figures 10, 11 and 12, the bubble size distributions are plotted on log-log plots in Figures 14 and 15 for analysis. While the central portions of each distribution appear to follow a power law, none of the scanned foamed cements have bubble size distributions that are exclusively governed by power law functions. The smallest bubbles in all the low-resolution cement scans do not appear to follow the power law trend of the median bubbles, as shown in Figure 14. For the 10, 20, and 30% foam quality cements the occurrence of small voids is less than the best fit power law relationship would predict, while the smallest voids in the 40% foam quality sample is greater than the best fit power law would predict. The smallest void spaces are all higher than the best fit power law prediction in the high-resolution scans shown in Figure 15. For these higher resolution scans this may be due to the restriction on amount and range of data points that comes with the much smaller sample. It is worth noting, that the higher the foam quality the more interconnected the bubble volumes are. With the digital CT scan data, bubbles

separated by a thin film of cement similar to the scan resolution are difficult or impossible to separate.

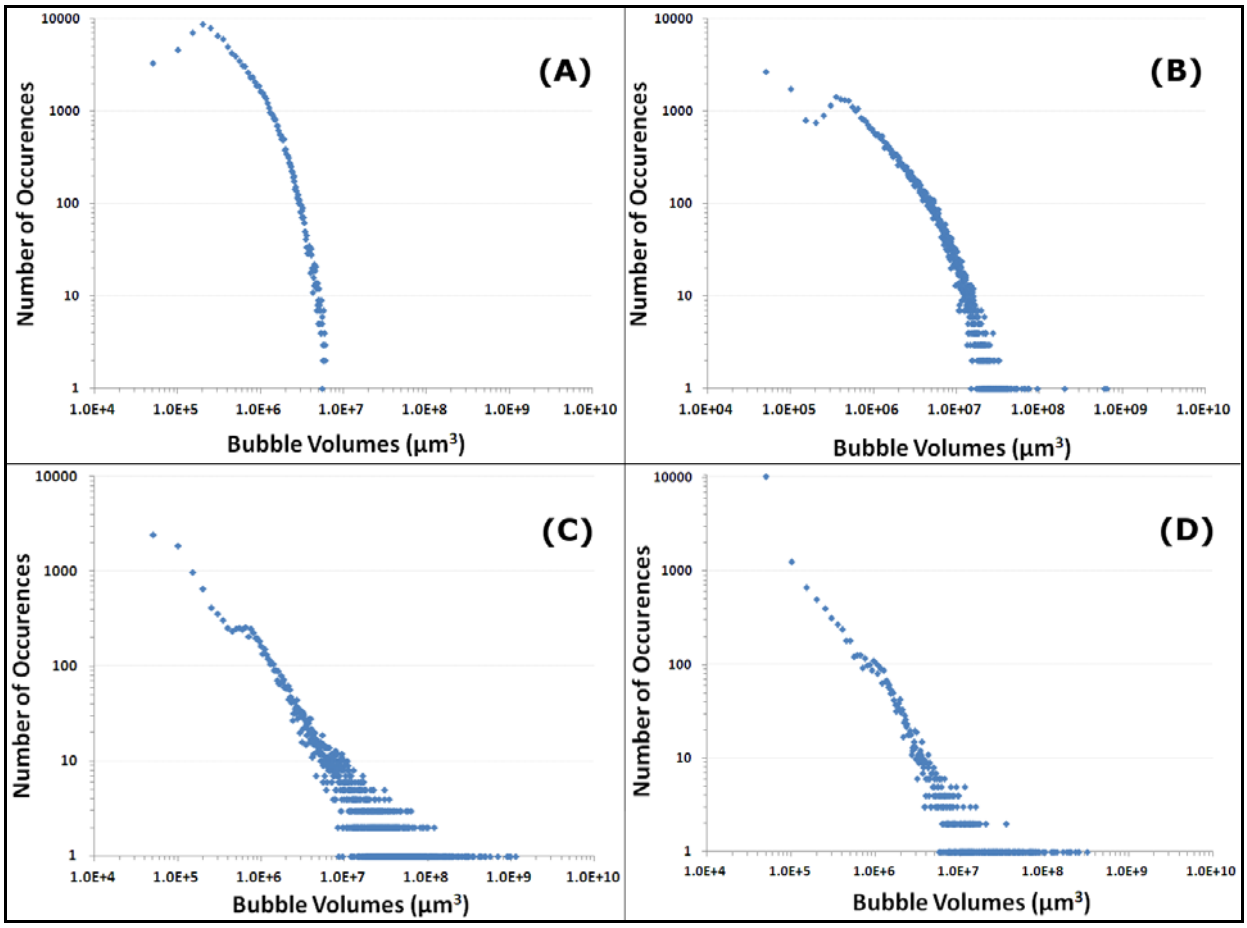

Figure 14: Log-log distribution of bubble sizes, scan resolution = 13.5 µm, bin size = 50,000 µm^3, volumes greater than 10^{10}µm^3 are not shown. Foam qualities shown are (A) 10%, (B) 20%, (C) 30%, and (D) 40%.

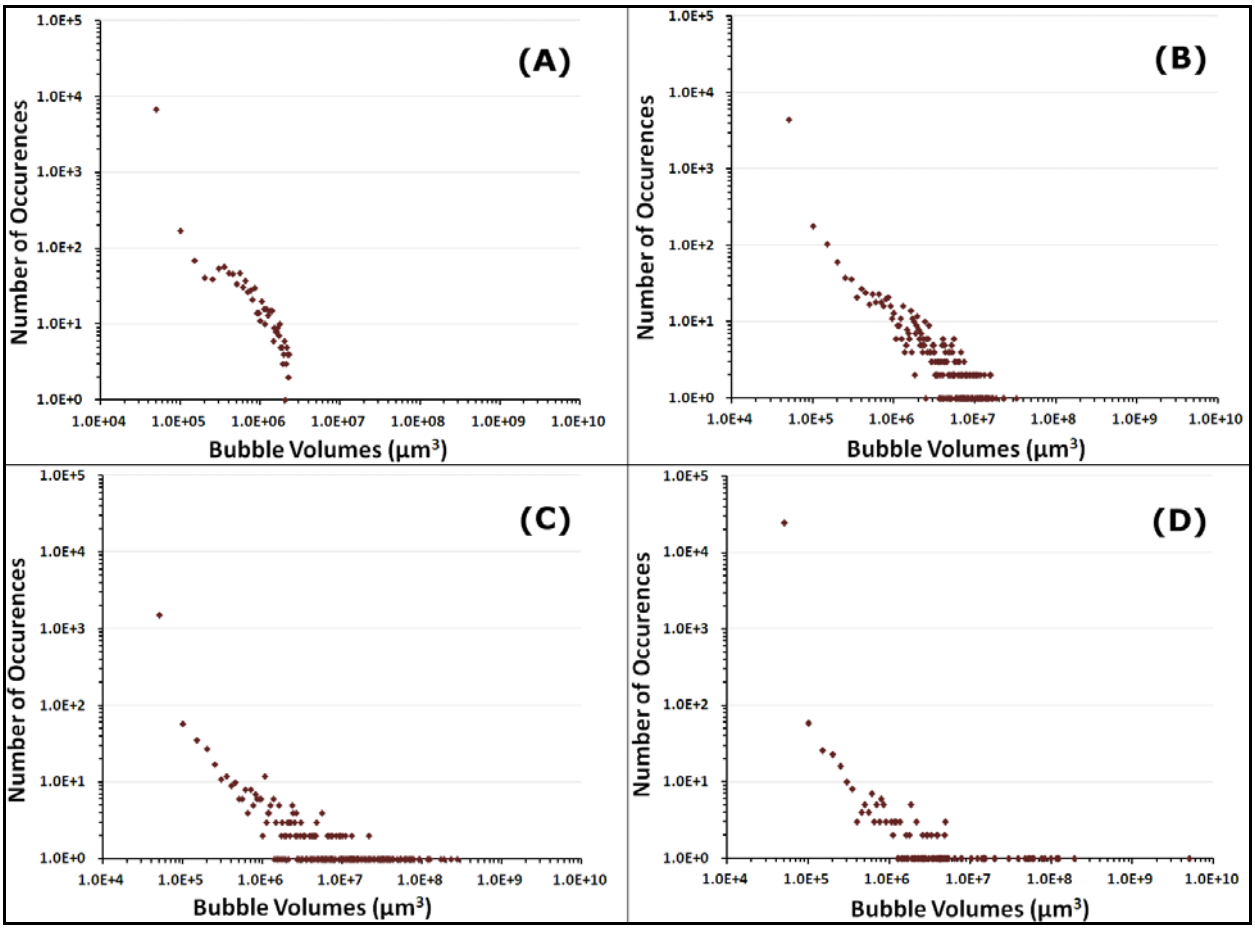

Figure 15: Log-log distribution of bubble sizes, scan resolution = 3.7 µm, bin size = 50,000 µm^3, volumes greater than 10^{10}µm^3 are not shown. Foam qualities shown are (A) 10%, (B) 20%, (C) 30%, and (D) 40%.

A (10.4 mm)^3 digital subsection of sample FCS1 10-21 was analyzed in detail to evaluate the 3-D distribution of different sized entrained bubbles. The scan analyzed has a 13 µm voxel resolution, which enabled a fairly large section to be analyzed. The analysis identified 169,607 individual bubbles and the range of sizes covered six orders of magnitude, from 5.22 to 2.2(10^{-5}) mm^3. The smallest size is the size of 10 connected voxels, all smaller values were removed as potential noise in this analysis.

A different way to visualize the BSD is to plot the volume of individual bubbles from the largest to the smallest (Figure 16). Figure 16 shows the distribution of individual bubbles in a (10.4 mm)^3 subsection of the 10% foam quality cement sample. The distribution of these bubbles has several interesting characteristics. There are very few large bubbles. As shown in Figure 16, the top 10% of the total void volume (red points) comprise only 0.7% of the total number of voids in this sample. The bubble volume quickly declines to a value on the order of 10^{-3} mm^3, with an average bubble size of 8.74(10^{-4}) mm^3. The smallest 50% of the bubbles (Figure 16, green data) are only 13.34% of the total gas volume in the sample.

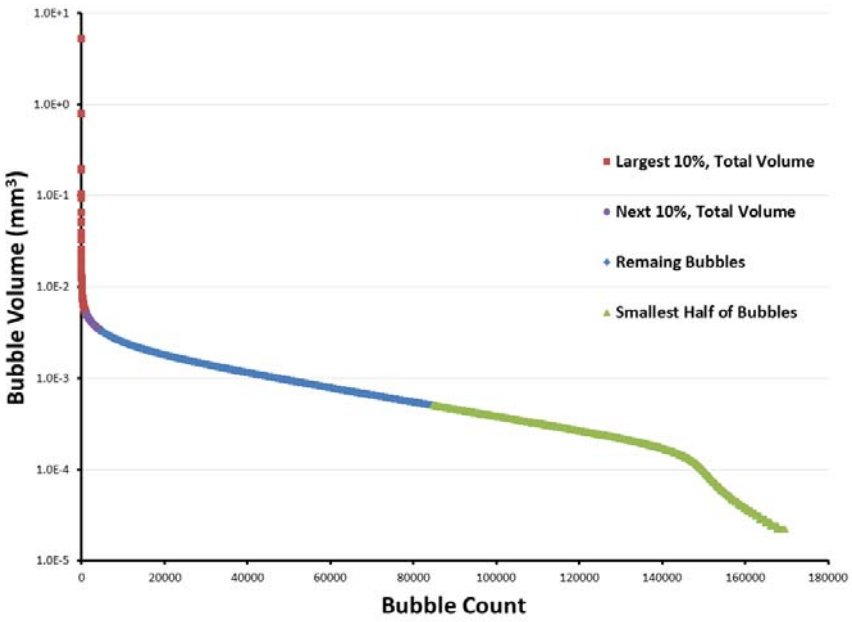

Figure 16: Distribution of individual bubbles in (10.4 mm)^3 subsection of the 10% foam quality cement sample. Largest 20% of the total void volume is shown as red and purple, smallest 50% of bubbles are shown in green, and the remaining bubbles are blue.

The distribution of these bubbles in 3-D space can be visualized with the CT data. The fully reconstructed volume is shown in Figure 17(A) as an opaque (10.4 mm)^3 cube. An orthoslice projection through the primary axes of the cube is shown in Figure 17(B), along with the largest bubbles in the sample, whose sum is 10% of the total void volume. These bubbles are shown separately in Figure 17(C), and several features can be noted. One large bubble in the forefront of the image is by far the largest in sample set; in fact it is 6.59 times greater in volume than the next largest bubble! The large bubbles are dispersed throughout the analyzed sample region, as can be noted by the ability to "see through" portions of the 3-D rendering in Figure 17(C). In addition many of these larger bubbles are actually multiple bubbles that have been connected together, either in post processing due to the threshold technique and the very small cement walls separating them, or because of the congealing of bubbles while the foamed cement was setting up. The next 10% of the total volume is shown in 3-D space in Figure 17(D). There are over three times more individual bubbles in this data set even though they comprise the same amount of void volume; 1,182 in the largest bubbles that are 10% of the total volume and 3,792 in the next 10% of the total volume. The smallest bubbles in the sample are shown in Figure 17(F). These are the smallest 84,803 of the individual bubbles; half of the total bubbles in the sample. The bubbles are well distributed throughout the region, but are so small that the edges of the cube in Figure 17(F) are again able to be "seen through". This half of the bubble set comprise only 13.34% of the total void space within the sample. The bubbles between the largest and the smallest are shown in Figure 17(E), and they too are well distributed throughout the sample. The ability to tease out this high level of detail from samples with a non-destructive CT scanning is a unique capability, and one that should provide insight into pressurized foamed cement samples in the near future.

A normalized breakdown of bubble sizes with respect to total volume of air is shown in Figure 18. For the 10% foam quality data shown in Figure 18(A) most bubbles are individual volumes.

The bubble distribution of 20% foam quality (Figure 18(B)) is similar, but there is some interconnectivity of entrained air pores, as can be noted by the increase in the largest bubble size in the distribution by an order of magnitude from the 10% values. For the 30% foam quality cement sample, 68% of total bubble volume is fully interconnected into a single pore network, as shown in Figure 18(C). This interconnected pore space rises to 98% of the total void volume in the 40% foam quality sample. Given the scale of bubble interconnectivity in cements with 30 and 40% foam qualities, the statistical analyses of their bubble size distribution must be viewed with caution, given that the bulk of the distributions are based on only 32% and 2% of the total bubble volume, respectively. In other words, the dataset on bubble sizes becomes less robust as connectivity increases, and bubbles can no longer be treated as separate entities.

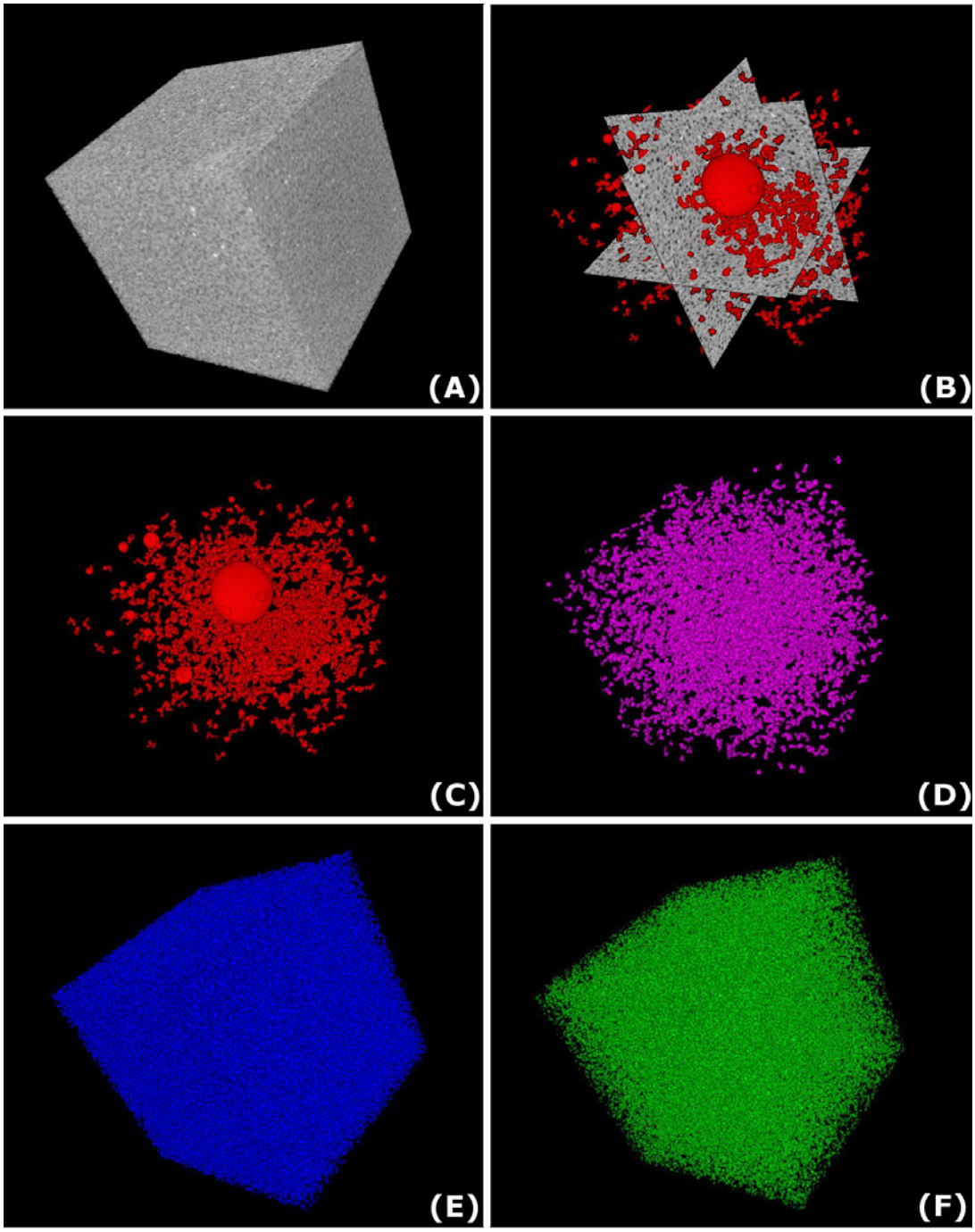

Figure 17: 3-D renderings of a (10.4 mm)^3 digital subsection of 10% foam quality cement sample. (A) Opaque grayscale cement cube. (B) Orthoslices of solid cube with largest bubbles. (C) Largest bubbles in dataset that sum to 10% of the total void space in the sample. (D) The next largest bubbles, summing again to 10% of the total void volume. (E) The mean bubbles, between the largest and the smallest in the sample set. (F) The smallest half of the bubbles.

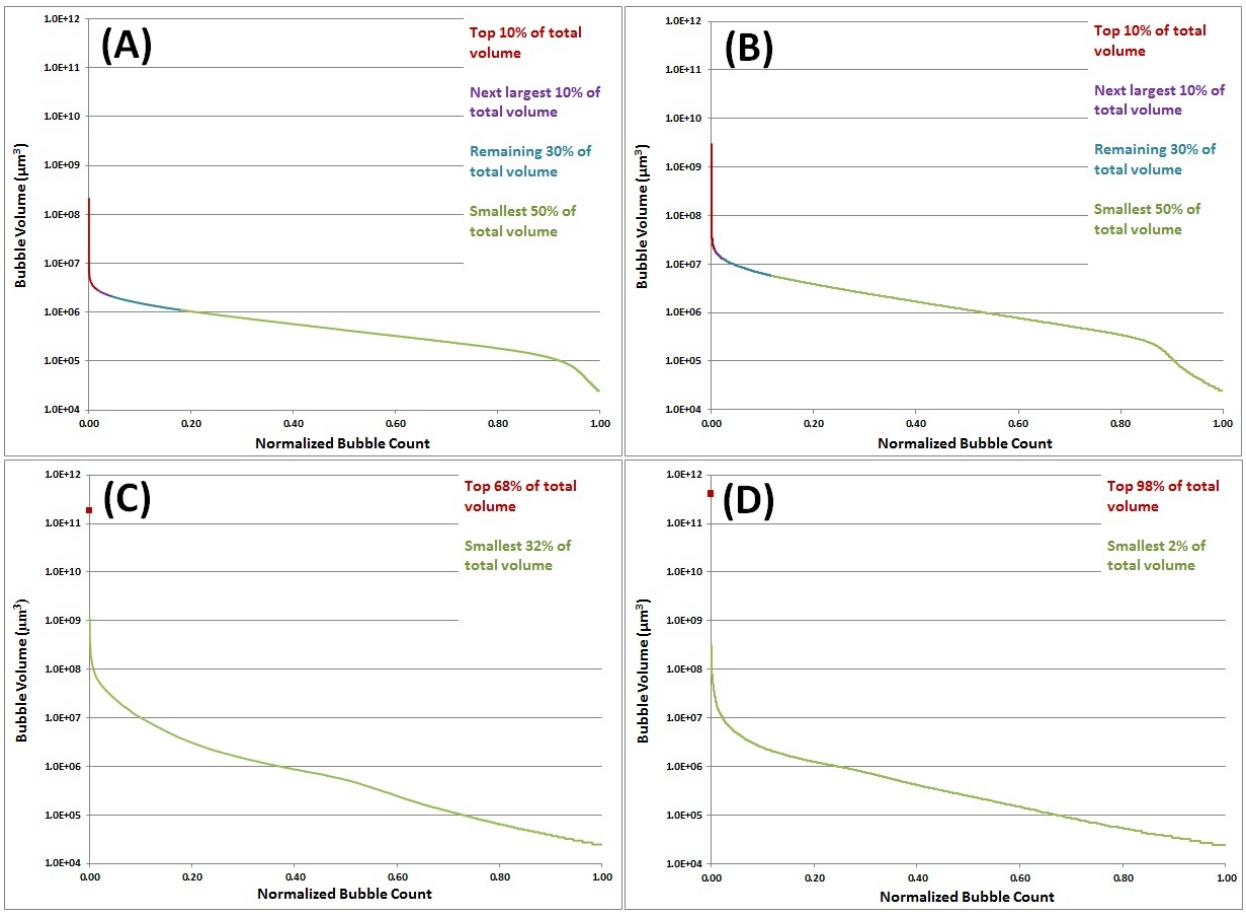

Figure 18: Normalized bubble size distributions in relation to total air volume. In higher entrained air cements, 30–40%, much of the bubbles are interconnected, forming one large pore structure. The remaining bubbles provide a less robust statistical tool for analysis of trends. Foam qualities shown are (A) 10%, (B) 20%, (C) 30%, and (D) 40%.

4. DISCUSSION

The use of CT imaging and statistical analysis provided a robust methodology for determining the quality, stability, and microstructure of foamed cement. The CT measured air volume was consistent with the foam quality of the cement samples. This consistency ensures that the CT derived image data is accurate and the stability of foamed cement systems can be readily determined. The stability of the cement can be seen in the both the images and the corresponding graphs. It can be seen that the higher the foam quality, the more interconnected the bubbles are. By definition, this increase in interconnectivity would correspond to a less stable cement. Bubble size distribution is typically used as an indicator of foamed cement stability. A stable foamed cement has a uniform distribution of distinct bubbles to ensure that gas will not break out of the slurry. The increase in size and interconnectivity of the bubbles infers an unstable foamed cement. Unstable foams can result in uncemented sections and ultimately loss of zonal isolation. Figure 18 shows a normalized bubble size distribution of all four foamed cement systems examined. From this graph we see a possible correlation between the slope of the curves and the stability of the cement. The profile is steepest for the 40% foam quality due to interconnected nature of bubbles.

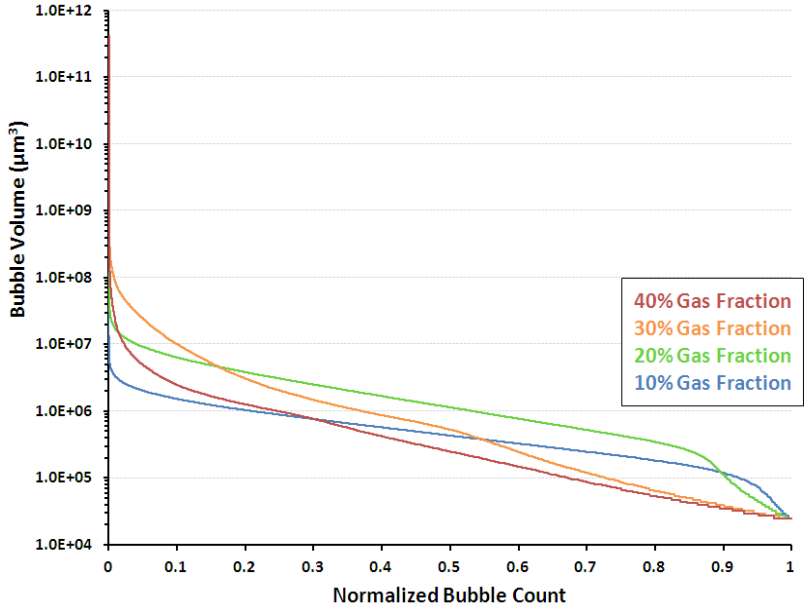

Figure 19: Normalized bubble size distributions in relation to total air volume: a comparison of foam qualities. Scan resolution = 13.5 µm.

Given the success of the atmospheric-generated foamed cement work, the next step is to apply this methodology to field-generated and pressure-generated foamed cements. A correlation between atmospheric-, field-, and pressure-generated foamed cement systems is desired to improve current testing methods and ultimately to develop stability profiles in the wellbore. This correlation will aid in a better understanding of the effects that foam cement production, transport downhole, and delivery to the wellbore annulus have on the overall sealing process. Ultimately, this research will provide researchers, regulators, and industry the knowledge to ensure the safe operation and integrity of wells in which foamed cement systems are used.

5. REFERENCES

API. *API Recommended Practice 10B-4. Recommended Practice on Preparation and Testing of Foamed Cement Slurries at Atmospheric Pressure, First Edition*; American Petroleum Institute: Washington, DC, 2004.

API. *API Recommended Practice 65-2. Isolating Potential Flow Zones During Well Construction, First Edition*; American Petroleum Institute: Washington, DC, 2010.

Arora, S.; Acharya, J.; Verma, A.; Panigrahi, P. K. Multilevel thresholding for image segmentation through a fast statistical recursive algorithm. *Pattern Recognition Letter* **2008,** *29,* 119–125. DOI:10.1016/j.patrec.2007.009.005.

Barrett, J. F.; Keat, N. Artifacts in CT: Recognition and Avoidance. *RadioGraphics* **2004,** *24,* 1679–1691. DOI:10.1148/rg.246045065.

Benge, G.; Poole, D. Use of foamed cement in deep water Angola. SPE/IADC Drilling Conference, Amsterdam, Netherlands, Feb 23–25, 2005.

Benge, O. G.; McDermott, J. R.; Langlinais, J. C.; Griffith, J. E. Foamed cement job successful in deep HTHP offshore well. *Oil and Gas Journal* **1996,** *94*, 58–63.

Bolte, S.; Cordelières, F. P. A guided tour into subcellular colocalization analysis in light microscopy. *J Microscopy* **2006,** 213–232. DOI: 10.1111/j.1365-2818.2006.01706.x.

de Rozieres, J.; Ferriere, R. Foamed-cement characterization under downhole conditions and its impact on job design. *SPE Production Engineering* **1991,** *6*, 297–304.

Frisch, G. J.; Graham, W. L.; Griffith, J. Assessment of foamed-cement slurries using conventional cement evaluation logs and improved interpretation methods. SPE Rocky Mountain Regional Meeting, Gillette, Wyoming, May 15–18, 1999; SPE 55649.

Griffith, J. E; Lende, G.; Ravi, K.; Saasen, A.; Nødland, N. E.; Jordal, O. H. Foam cement engineering and implementation for cement sheath integrity at high temperature and high pressure. IADC/SPE Drilling Conference, Dallas, TX, March 2–4, 2004; SPE 87194.

Harlan, T. D.; Foreman, J. M.; Reed, S. D.; Griffith, J. E. Foamed cement selection for horizontal liners proves effective for zonal isolation—case history. SPE Rocky Mountain Petroleum Technology Conference, Keystone, CO, May 21–23, 2001; SPE 71055.

Harms, W. M.; Febus, J. S. Cementing of fragile-formation wells with foamed cement slurries. *Journal of Petroleum Technology* **1985,** *37*, 1049–1057.

Hover, K. C. The influence of water on the performance of concrete. *Construction and Building Materials* **2011,** *25*, 3003–3013. DOI: 10.1016/j.conbuildmat.2011.01.010.

Judge, R. A.; Benge, G. Advances in metering and control technology improves design and execution of foamed cement jobs. IADC/SPE Asia Pacific Drilling Technology, Jakarta, Indonesia, Sept 7–9, 1998; IADC/SPE 47831.

Kopp, K.; Reed, S.; Foreman, J.; Carty, B.; Griffith, J. Foamed cement vs. conventional cement for zonal isolation – case histories. SPE Annual Technical Conference and Exhibition, Dallas, TX, Oct 1–4, 2000; SPE 62895.

Kutchko, B.; Pike, W.; Lang, K.; Strazisar, B.; Rose, K. An assessment of research needs related to improving primary cement isolation of formations in deep offshore wells; NETL-TRS-3-2012; EPAct Technical Report Series; U.S. Department of Energy, National Energy Technology Laboratory: Morgantown, WV, 2012; p 20. http://netl.doe.gov/onsite_research/

Milojević, S. Power-law Distribution in Information Science—Making the Case for Logarithmic Binning, *J. American Society for Information Science and Technology* **2010,** *61*, 2417–2425. DOI: 10.1002/asi.v61:12.

Mindess, S.; Young, J. F. *Concrete.* Prentice-Hall: Englewood Cliffs, NJ, 1981; p 671.

Moore, S.; Miller, M.; Faul, R. Foam cementing applications of a deepwater subsalt well—case history. IADC/SPE Drilling Conference, New Orleans, LA, Feb 23–25, 2000; IADC/SPE 59170.

Osuna-Enciso, V.; Cuevas, E.; Sossa, H. A comparison of nature inspired algorithms for multi-threshold image segmentation. *Expert Systems with Applications* **2013,** *40*, 1213–1219. DOI:10.1016/j.eswa.2012.08.017.

Nelson, E. B., Ed. *Well Cementing*; Schlumberger Educational Services: Sugar Land, TX, 2006.

Rae, P.; Lullo, G. D. Lightweight cement formulations for deep water cementing: Fact and fiction. SPE Annual Technical Conference and Exhibition, Houston, TX, Sept 26–29, 2004; SPE 91002.

Rasband, W. S.; ImageJ. http://imagej.nih.gov/ij/ (accessed 2012), U.S. National Institutes of Health: Bethesda, MD, 1997–2012.

Thayer, R. D.; Ford, D. G.; Holekamp, S.; Pferdehirt, D. J. Real-time quality control of foamed cement jobs: A case study. SPE Annual Technical Conference and Exhibition, Houston, TX, Oct 3–6, 1993; SPE 26575.

Taiwo, O.; Ogbonna, J. Foam cementing design and application: A cure for low gradient-associated problems in deepwater operations in the Gulf of Guinea. Nigeria Annual International Conference and Exhibition, Abuja, Nigeria, July 30–Aug 3, 2011; SPE 150767.

White, J.; Moore, S.; Miller, M.; Faul, R. Foaming cement as a deterrent to compaction damage in deepwater production. IADC/SPE Drilling Conference, New Orleans, LA, Feb 23–25, 2000; IADC/SPE 59136.

The National Energy Technology Laboratory (NETL) conducts cutting-edge energy research and technology development and analyzes energy systems and international energy issues for the U.S. Department of Energy. The NETL-Regional University Alliance (NETL-RUA) is an applied research collaboration that combines NETL's energy research expertise with the broad capabilities of five nationally recognized, regional universities: Carnegie Mellon University (CMU), The Pennsylvania State University (PSU), University of Pittsburgh (Pitt), Virginia Polytechnic Institute and State University (VT), and West Virginia University (WVU), and the engineering and construction expertise of an industry partner (URS). The NETL-RUA leverages its expertise with current fossil energy sources to discover and develop sustainable energy systems of the future, introduce new technology, and boost economic development and national security.

Brad Tomer
Acting Director
Strategic Center for Natural Gas and Oil
National Energy Technology Laboratory
U.S. Department of Energy

Maria Vargas
Deputy Director
Strategic Center for Natural Gas and Oil
National Energy Technology Laboratory
U.S. Department of Energy

Roy Long
Technology Manager
Strategic Center for Natural Gas and Oil
National Energy Technology Laboratory
U.S. Department of Energy

Elena Melchert
Program Manager
Oil and Gas Production
Office of Fossil Energy
U.S. Department of Energy

Cynthia Powell
Director
Office of Research and Development
National Energy Technology Laboratory
U.S. Department of Energy

Timothy McNulty
Associate Vice-President for
Government Relations
Carnegie Mellon University

Henry Foley
Vice President for Research
The Pennsylvania State University

George Klinzing
Vice Provost for Research
University of Pittsburgh

Robert Walters
Vice President for Research
Virginia Polytechnic Institute and State
University

Fred King
Vice President for Research and
Economic Development
West Virginia University

Kevin Donovan
RES Program Manager
URS Corporation

NETL Technical Report Series